UV spectral measurements at moderately high resolution and of OH resonance scattering resolved by polarization during the MANTRA 2002–2004 stratospheric balloon flights

D.W. Tarasick [a,*], D.I. Wardle [a], C.T. McElroy [a], C. McLinden [a], S. Brown [b], B. Solheim [b]

[a] Air Quality Research Division, Environment Canada, Downsview, ON, Canada M3H 5T4
[b] Solar Terrestrial Physics Laboratory, Centre for Research in Earth and Space Science, York University, 4700 Keele Street, Toronto, Ontario, Canada M3J 1P3

ARTICLE INFO

ABSTRACT

A moderately high-resolution (<0.1 nm) grating spectrometer designed to measure the solar radiation in the spectral range 295–315 nm was flown on the MANTRA stratospheric balloon payloads of 2002 and 2004. The instrument measures both the direct sunlight and the radiation scattered by the atmosphere. The latter can be observed in two orthogonal polarization directions, at $90°$ from the solar azimuth and at several elevations above the horizon. As the OH molecule is the principal resonant scatterer in this spectral region, this permits the inference of both ozone and OH column amounts as well as limited profile information. This paper describes the instrument and its in-flight characterization, the basic data processing and the influence of several aspects of the flight profile. The direct sun measurements are analyzed both to characterize the spectrometer responsivity to scattered radiation and to estimate the ozone abundance at the flight altitude and above. An example of a high-resolution solar spectrum at 37 km altitude is presented and compared with others in the literature. The measured OH and Rayleigh-scattered spectra are used to derive OH radiation intensity measurements (the OH airglow), which are compared with others in the literature.

Crown Copyright © 2008 Published by Elsevier Ltd. All rights reserved.

1. Introduction

The hydroxyl radical is the most important oxidizing agent in the middle atmosphere, and OH chemistry dominates ozone destruction above about 40 km [1]. However, its measurement is quite challenging and for this reason there exist relatively few observations of the atmospheric concentration of this important trace species. Measurements of solar radiation scattered by OH in the $A\,^2\Sigma$–$X\,^2\Pi$ (0–0) band at 308 nm have been made in the upper stratosphere and mesosphere by rocket [2] and balloon-borne spectrometers [3,4]. The MAHRSI instrument on the space-shuttle-deployed CRISTA-SPAS satellite, also a UV spectrometer operating in the 308-nm range, produced several thousand OH profiles between about 45 and 80 km altitude, during two short periods in 1994 and 1997 [5,6]. These measurements proved difficult to reconcile with standard models of HO_x chemistry [7–9]. The $A\,^2\Sigma$–$X\,^2\Pi$ (0–0) transition is also the basis of OH measurements using balloon-borne lidar [10] and laser-induced fluorescence [11]. Measurements have also been made with balloon-borne IR interferometers, using the thermal emission of OH [12,13]. More recently the Microwave Limb Sounder (MLS) instrument on the Aura satellite, launched in 2004, has the capability to measure OH between about 20 and

---

60 km altitude using thermal emission from 2.5 THz rotational lines in the ground vibrational state, and a similar instrument has been flown on a balloon [14]. These more recent measurements and analyses appear to resolve the difficulties presented by the MAHRSI measurements, although at the cost of assuming an unknown mechanism for ozone production above 40 km [15,16].

The UV spectrometer described here was designed to observe the $A\ ^2\Sigma–X\ ^2\Pi$ (0–0) scattered emission of OH from a stratospheric balloon. An early version was first flown in 1975 and 1977 on the Canadian Stratoprobe payloads launched from Yorkton, Saskatchewan and Palestine, Texas. These measurements, which very clearly identified the $A\ ^2\Sigma–X\ ^2\Pi$ radiation, have been briefly described previously [3].

The unique design of this instrument includes the capacity to significantly reduce the interference of Rayleigh-scattered light by changing the instrument's polarization. Other design features are moderately high spectral resolution (<0.1 nm), light weight, and high light-gathering power. The instrument carries an onboard data collection and control computer, and is capable of independent, automated operation as well as of remote control by telemetry.

The data presented here were obtained during the MANTRA balloon flights of September 3, 2002 and September 1, 2004.

2. Instrument design and operation

The spectrometer layout is of the most simple Ebert–Fastie type [17]. With the exception of the foreoptics, the instrument design (although larger, and having consequently higher resolution) is similar to that of the Brewer ozone spectrophotometer, also developed in our laboratory.

A unique feature of the instrument is the foreoptics, which are contained in a cylinder that can be rotated about its axis in order to change the polarization of the measurement. The first element is a 25-mm Glan–Taylor prism polarizer. When the instrument is properly pointed at 90° to the sun, by rotating the foreoptics the polarizer can be set to admit light polarized either in, or perpendicular to the scattering plane determined by the sun. The former position will greatly reduce the amount of Rayleigh-scattered light detected, since this is strongly polarized in the perpendicular direction. The Rayleigh background is much larger than the OH emission, but by this method its signal is reduced, relative to that of the OH, by as much as a factor of 16. To our knowledge this technique has not been used in other measurements of the $A\ ^2\Sigma–X\ ^2\Pi$ (0–0) OH band [2–6].

Following the polarizer, a 1/4 wave plate is set so that, in combination with the prism, it causes the light entering the spectrometer proper to be completely circularly polarized, given that the incident light has essentially no circular polarized component (Stokes parameter $V = 0$), as is the case for light from the sun or sky [18,19]. Detailed multiple scattering calculations for our viewing situation indicate a degree of circular polarization for the incident light of about 10^{-5}.

The remainder of the foreoptics consists of an aperture stop of diameter 25 mm, and a lens of focal length 200 mm, which is approximately that distance in front of the entrance slit. A small transfer lens, 15 mm in front of the entrance slit, produces an image of the aperture stop, approximately 75 mm in diameter, on the grating.

A filter wheel, located in the gap between the transfer lens and the entrance slit, allows two different neutral density filters or an opaque shutter to be rotated into the light path.

The overall instrument aperture is $f/8$, as determined by the aperture stop. At this aperture there is no significant change in focus over the 300–315 nm range. Ray-tracing analysis indicates the aberration-limited bandpass to be asymmetrical, with rms width 0.010 nm and full width at half-maximum 0.014 nm, while the astigmatism is 0.014 nm. These factors, as well as physical imperfections and focusing errors raise the actual bandpass from the 0.055 nm determined by the physical slit widths to about 0.81 nm (as measured by onboard calibration).

Attached to the foreoptics tube is a coaxial extension projecting ∼220 mm outside the box containing the spectrometer. The coupling is rigid but made easily breakable so as to limit damage to the main optics during rough landings of the balloon payload. The extension, which rotates with the foreoptics, carries two pairs of photodiodes for detecting the elevation of the sun and a Teflon reflective diffuser that can be moved in front of the tube opening to diffusely reflect either light from the sun or from a mercury discharge lamp into the spectrometer. The mercury lamp is also mounted on the outside of the box and permits frequent wavelength calibration. The photodiode pairs are mounted 90° apart and aligned with the two polarizing directions defined by the Glan–Taylor prism. The fields of view of the diodes in each pair are arranged so that their exposures are equal when they point at the sun and fall off rapidly in one direction and slowly in the other, in opposite sense for each member of the pair. This allows the foreoptics rotation to be set so that the spectrometer measures either with polarization in the direction of the sun or perpendicular to it, with an accuracy of a few degrees.

The instrument is mounted on a cradle which allows it to be tilted between about 2 and 9° above the horizontal. It is designed to fly on a balloon payload with solar tracking, so it flies in a fixed orientation with respect to the solar azimuth, pointing to the sky 90° to the west of the sun and at an elevation determined by the cradle. The actual elevation of the spectrometer is monitored by an onboard clinometer with a precision of 0.02° and an estimated accuracy of 0.04°. There is, in addition, an uncertainty of 0.2° in the alignment of the spectrometer frame to its viewing direction.

The basic time unit in the operation is 8 ms, effected by a 125 Hz interrupt from the onboard computer. At each interrupt a counter that is driven by the prescaler on the photomultiplier (PMT) is read and the wavelength drive motor is commanded to take one step. All other tasks are done in the background. This includes reading signals from thermistors, LED–photodiode pairs, microswitches and potentiometers used to control the four DC motors associated with cradle

elevation, polarization, and positions of the filter wheel and diffusing screen, and also recording this and other housekeeping data. A typical wavelength scan from 306 to 310 nm, at 125 steps s^{-1}, takes about 28 s. Scans are typically made in pairs, forward and reverse, in order to maximize observing time. Each scan produces a spectrum comprising a set of counts, each accumulated for 8 ms, at each step in the scan. In each scan, step positions increase or decrease monotonically by single-step increments from the initial position to the final position.

Command sequences during flight (Table 1) included measurements of the solar spectrum ("sun scans") and that of the mercury lamp ("Hg scans"), both via the diffusing screen, dark counts, and with no diffuser, measurements of the sky radiation for OH. The last were composed of scans made with the foreoptics rotation set to pass radiation polarized in the direction of the sun (the "weak" polarization) and of scans made with the foreoptics rotation set to pass radiation polarized perpendicular to the direction of the sun (the "strong" polarization). Each OH measurement group is a group of ten scans, two sets of four "weak" scans bracketing two "strong" scans. This takes about 6 min and is subsequently analyzed to give a single measurement of the OH integrated signal. A full sequence of OH measurements comprises eight such series, effected at different cradle elevations. Four cradle elevations were used, at approximately 2.8, 3.7, 5.4, and 8.0. The sequence started at the lowest, ramping up to the highest and then down again. Sun and Hg lamp scans were done at the beginning of each sequence, and dark measurements were made three times per sequence. The duration of the full OH sequence was about 55 min.

3. Flight profiles

The data presented here were obtained during two flights of the instrument on the MANTRA balloon payload, on September 3, 2002 and September 1, 2004.

The M2002 launch time was 08:01 UTC (02:01 CST, local time), the ascent being in darkness. Float altitude of 37.5 km was attained at 10:45 when the solar elevation was $-12°$. Float altitude was reduced slightly on two occasions during the day by $\sim$3 km. The maximum solar elevation was 44.6°. The flight was terminated just after sunset when the solar elevation was $-6°$, at 02:00 UTC, by releasing the gondola from the balloon. The launch point was at 52.02°N, 107.03°W and termination of the flight occurred when the balloon was at 52.27°N, 100.99°W.

The M2004 ascent was in daylight: lift-off time was 14:33 UTC (08:33 CST, local time), when the solar elevation was 19°. The end of the rise and the maximum altitude, 37.35 km, occurred at 17:31 UTC when the solar elevation was 42°. Maximum solar elevation was 46.1°. The flight continued through the day, losing altitude slowly until 02:40 UTC, when the altitude was 32.5 km and solar elevation $-7°$, at which time the gondola was released from the balloon. The launch point was the same as M2002 and termination of the flight occurred when the balloon was at 51.43°N, 108.44°W.

The spectrometer operated satisfactorily, in general, on both flights. Problems with the payload azimuth control system, and (on M2004) loss of command telemetry unfortunately rendered more than 50% of the data unusable. Nevertheless, from the periods when the azimuth control was operative, we are able to derive useful measurements of the solar UV spectrum at altitude, the amount of ozone above the balloon during the M2002 flight, and the OH radiance. In addition, as shown below, some of the solar scans affected by minor misorientation of the payload can be corrected using the payload's magnetometer data.

4. Instrument characterization and data reduction

The data as recorded in some 700 scans for each flight have been examined for quality and used to characterize the spectrometer in flight.

4.1. Counting statistics

The raw spectrometer data consist of series of photoelectron counts organized in wavelength scans. We examine the noise characteristics of the data by comparing the value of each count, c, with the average $\bar{c}$ of its 12 nearest neighbors, noting that the emission of photoelectrons under a constant irradiance follows Poisson statistics. Typical signals for the different scan types are: sun ($\bar{c} \cong 5000$); strong ($\bar{c} \cong 100$); weak ($\bar{c} \cong 5$); dark ($\bar{c} \cong 2$); Hg lamp ($\bar{c} \cong 1200$). The parameter $p = |c - \bar{c}|/\sqrt{c+1}$, which is essentially the ratio of individual deviations from the mean to their expected standard deviation, was calculated for each count. (We use $c+1$ rather than $\bar{c}$ in the denominator for better handling of low values of c.) The averaging width is small compared with the spectral passband, so the statistics of p are not strongly affected by the form of the measured spectrum.

Noting that c is the result of counting the output from the prescaler (which divides the photon count by four) and assuming Poisson photocounts, calculated expectation values for p lie between 0.30 and 0.41 for all count totals greater than one. A very small number of counts have large p values; these are statistical outliers, probably resulting in most cases from the detection of cosmic rays. We therefore reject counts for which $p > 2.5$ and replace them with the neighbour average values. This is a rather strong criterion for rejection; out of the several million counts on each flight no exceedances $p > 2.5$ should be observed, for Poisson photon statistics and constant signals. This rejection procedure removes

$\sim$150 counts. These outliers were apparently random with a mean rate of occurrence about ten per hour and they had a negligible effect on the data.

The detection linearity or dead time determination was made by comparing several adjacent pairs of solar scans with different attenuator settings. For Poisson counts the counting rate can be expressed to first order as $n = n_0(1 - n_0\tau)$, where n is the observed and n_0 the true count rate, and τ is the dead time. Dead time was determined to be 37 ± 2 ns (1σ). Although this nonlinearity was significant only for the sun scans, all counts were corrected for dead time.

4.2. Wavelength calibration and slit function

Although the wavelength scan mechanism, with the grating rotation defined by crossed wires, is designed to minimize hysteresis in the wavelength setting, there remains a small amount in the stepping motor/micrometer linkage. By comparing pairs of forward and reverse scans of the mercury lamp, the sun and the strong skylight, "backlash" was determined to be nearly always two steps (0.003 nm), and all scans were correspondingly adjusted. Following this, the offset of each of the spectra was established; that is, the shift (in steps) of the spectrum required to bring the wavelengths of known lines into their correct positions. For the strong and sun scans this could be done directly, while for the weak scans an offset was determined by linear interpolation from the sun, strong or mercury lamp scans that bracketed them. This was facilitated by the fact that most of the Hg lamp scans also contained the solar spectrum. This allowed the wavelength assignment of the main Hg lines to be transferred to the sun scans, and thence to the strong sky scans.

The key mercury lines were the 312.567 nm line of the 313 nm triplet, and the 302.150 nm line of the 302 nm quartet, as well as, in M2004, the singlet 296.728 nm line. One sun scan (#216 in M2002, #442 in M2004) was chosen as the reference, and the other scans were shifted to maximize the correlation with the reference scan. In order to verify that a single shift of steps would allow the same steps-to-wavelength relation to apply to all scans, this was also done on single 2-nm segments (centered on roughly 302, 308, and 312 nm), which were separately shifted to maximize the correlation with the corresponding segments of the reference scan. In all cases the required number of steps for each of the three segments differed by no more than two steps (0.003 nm), and the interval between the two main mercury lines remained constant to the same degree.

The weak scans are all made within 2.5 min of a strong scan and nearly all are bracketed by scans with offsets that are less than five steps different. Since all of the strong scans were found to have self-determined shifts with a precision of two steps or better, one may conclude that the maximum uncertainty in the shift is five steps.

The design of the wavelength scan mechanism is such that the wavelength dispersion changes slightly over the scanning range. Characterizing this for M2004 was simple because the long scans included the isolated line at 296.728 nm and a quadratic dispersion curve could be derived from the fit to the three main lines. As the M2002 Hg scans did not include the 296 nm singlet, a single Hg scan uncontaminated by sunlight was used to derive a local dispersion from the four lines in the 302 nm group. A local linear dispersion was similarly obtained for the 313 nm triplet, except that as the lines at 313.155 and 313.184 nm are not resolved, the relative strength of these lines was an additional fitting parameter, and the fit used data from 22 Hg scans. The calculated linear dispersions at 302 and 313 nm were different, and consistent with the curve derived from the M2004 data. The maximum correction, with respect to the wavelength assignment that would be derived from a linear fit between 302 and 313 nm, is 0.021 ± 0.004 nm (1σ) and occurs at the midpoint ($\sim$307.5 nm). Combining the errors in this, in the shift and the much smaller uncertainties in the linear dispersions gives an overall maximum error of 0.010 nm in the wavelength setting for M2002 and 0.007 nm for M2004.

The instrument slit functions during M2002 at 302 nm and 313 nm are shown in Fig. 1. Each is the mean of several scans of the mercury calibration source. Since differences between them are slight, and the 313 nm version was measured with somewhat greater precision and more frequently, it was used in this analysis. Slit functions determined during M2004 (also shown) are again not significantly different, and so the same slit function was used throughout.

4.3. Sensitivity to azimuth pointing error

During M2002 more than two dozen sun scans from 298.5 to 311.5 nm were recorded, over a range of solar elevation and balloon altitude. Despite the malfunction of the azimuth pointing system, during about ten of these scans the azimuth pointing error stayed within $\pm 2^\circ$. This permits us to determine the ozone column above the balloon at these times. During several others the pointing error varied slowly, by less than 20° through the scan. While the spectra from these scans are plainly affected by the azimuth error, it is possible to derive an acceptable correction by estimating the dependence of signal on pointing error, using other scans during when payload was rotating more rapidly.

Information about the orientation of the instrument is available from an onboard magnetometer. Unfortunately the magnetometer response to a change in azimuth was not linear, presumably because of magnetization of the payload. This nonlinearity was calibrated by assuming that when the rotation rate was greater than 2 rpm the angular acceleration of the payload changed only slightly during any one rotation. The times when the magnetometer signal crossed a particular value were taken to define the periods of rotation, and the angular motion within any period was computed from the times of the beginning and ending crossings as well as the previous and next crossings, assuming a constant rate of change of
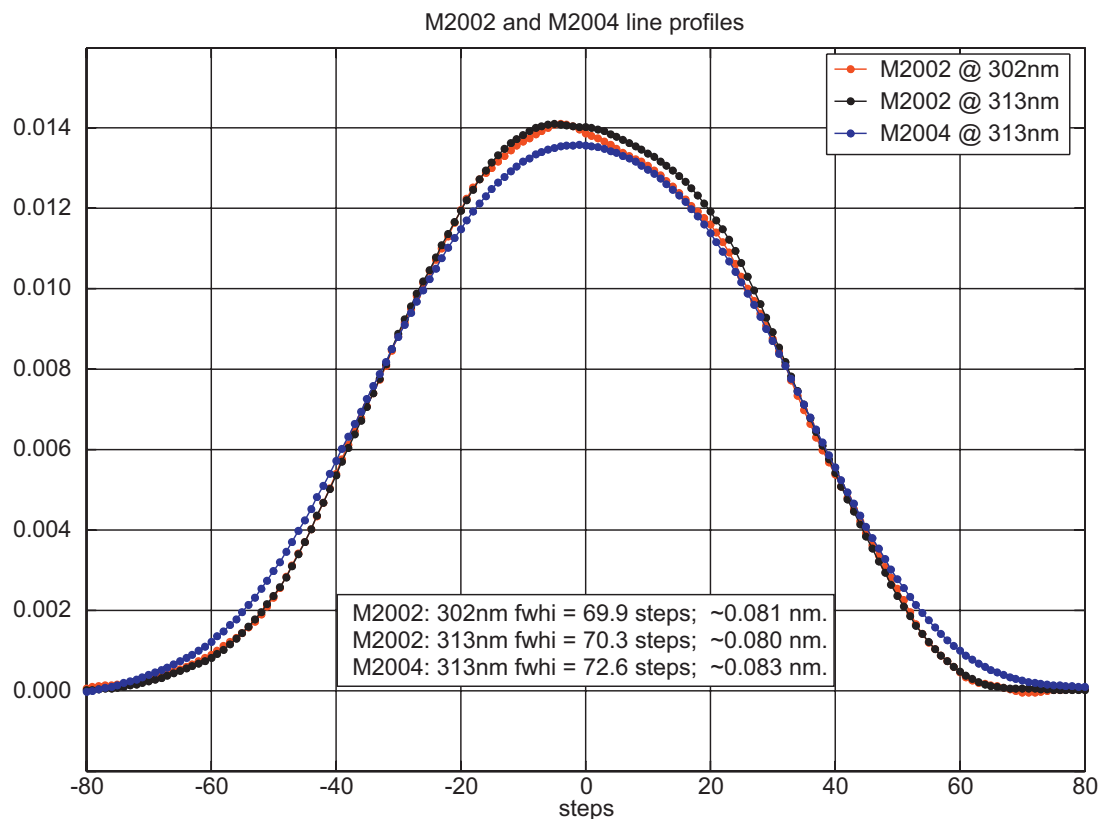
M2002 and M2004 line profiles

Fig. 1. Instrument slit functions at 302 and 313 nm.

acceleration. A point during sunset (solar zenith angle ~93°, azimuth 286.6°) when the payload azimuth control was functioning correctly was used as an initial reference point. The change in magnetic declination, obtained from the Canadian Geological Survey, is significant (~ 3.5°) over the flight duration of M2002 and is taken into account. The resulting mean calibration curve shows good agreement with the sunset point and three other reference points when the payload was accurately pointed. From this and the spread of values obtained from the 96 payload rotations, we conclude that the uncertainty in the corrected magnetometer signal is about 1° (1σ) over the range of azimuth used in the following analysis.

During one of the sun scans (#102) the payload made more than two complete rotations, yielding two complete tracings of the azimuth response within a range of only 2 nm. Given the relatively high solar elevation, this makes correction for differential ozone absorption unnecessary, and the ratio of this spectrum to another with negligible azimuth error gives response versus step number, or equivalently, response versus time. This can be converted to response versus azimuth error derived from the magnetometer signal, as long as the spectrometer time and the magnetometer time were precisely synchronized. In fact they were different by several seconds; however, it was possible to determine this difference precisely by observing the shadows of a wire and a vertical strut on the payload, which appeared in the data whenever the payload azimuth pointing was in error by about 10 or 20°, respectively. A scan made when the payload was oscillating slowly (#501) allowed the time offset to be fixed because the shadows must be at the same angle regardless of the direction of rotation. This in turn fixed the azimuth location of the shadows, allowing a time offset to be determined for any scan in which the shadows appear. Fig. 2 shows the result of this procedure applied to the two relevant parts of scan #102; the two azimuth response functions agree quite well. Their smoothed mean, also shown, is used in the corrections described below. The time offset throughout the flight was assumed to have a linear trend computed from the scan #102 and #501 values (2 and 3.5 s).

5. Ozone retrievals

The direct sun measurements were put in the schedule in part because of the anticipated dependence of the OH signal on the ozone at float altitude and above. The sun measurements should allow better estimates of ozone than available from either the onboard ozonesonde (which was expected to exhaust its sensing solution before, or not long after the payload reached float altitude) or climatology.

As indicated in Table 2, the 13 useful sun scans cover a range of solar zenith angles (SZA), making it possible to do a Langley-plot extrapolation to accurately estimate the extraterrestrial spectrum, via which ozone above the balloon may be
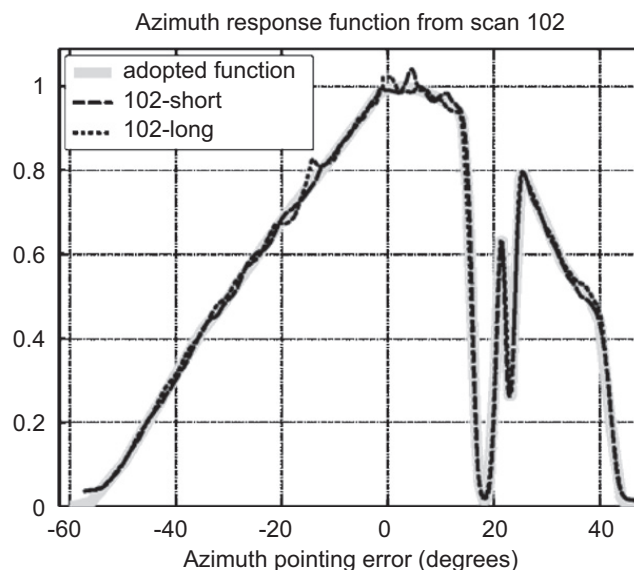
Fig. 2. Two response versus azimuth error functions obtained from scan #102. During this sun scan the payload made more than two complete rotations, allowing the azimuth sensitivity to be derived accurately.

Table 1
Observation sequences used in M2002 and M2004

Name	Flight	λ_{low} (nm)	λ_{high} (nm)	Polarization	Filter	Screen	Duration (s)
Weak	2002	305.9	309.8	Weak	None	Out	27
Weak	2004	306.0	310.9	Weak	None	Out	34
Strong	2002	305.9	309.8	Strong	None	Out	27
Strong	2004	306.0	310.9	Strong	None	Out	34
Sun[a]	2002	298.0	314.8	Strong	Various	In	Up to 136
Sun[a]	2004	294.3	313.8	Strong	Various	In	Up to 136
Hg[a]	2002	298.0	314.8	Hg	Various	In	Up to 136
Hg[a]	2004	294.3	313.8	Hg	Various	In	Up to 136
Dark		Not relevant		–	Opaque	–	14

[a] These are the full wavelength ranges in each flight. There were "short" and "long" scan versions of the lamp and sun, both in 2002 and 2004.

Table 2
Ozone slant columns amounts relative to the mean from scans #392 and #393 with rotation and regression 1σ uncertainties

Scan	P (Pa)	μ	L1 ozone			L2 ozone		
			O_3 (DU)	Az. error	Reg. error	O_3 (DU)	Az. error	Reg. error
#108	421	1.73	1.96	0.03	0.68	3.46	0.12	2.90
#109	425	1.72	0.92	0.00	0.67	3.21	0.01	2.85
#110	429	1.71	1.90	0.06	0.74	1.74	0.34	3.14
#111	429	1.70	0.88	0.01	0.57	2.94	0.23	2.41
#209	474	1.46	0.30	0.08	0.51	2.60	0.46	2.16
#216	474	1.44	0.70	0.11	0.49	2.42	0.32	2.05
#217	474	1.43	0.39	0.33	0.48	2.92	0.25	2.00
#392	479	1.50	0.47	0.04	0.26	0.55	0.38	1.12
#393	488	1.51	−0.57	0.07	0.26	−0.57	0.22	1.12
#480	571	1.66	−11.15	0.00	0.49	−8.39	0.00	2.08
#481	569	1.67	−11.38	0.00	0.48	−9.86	0.00	2.03
#611	693	3.46	−80.10	0.44	0.58	−79.58	0.99	2.45
#612	693	3.52	−81.24	0.50	0.57	−78.84	1.15	2.41

derived from each sun scan. On M2004 payload malfunctions allowed too limited a span of solar elevation in the available scans to allow a useful determination of the total ozone above the balloon.

   Ideally, the differences between solar spectra should be attributable only to differences in the amount of ozone along the slant path between the spectrometer and the sun at the measurement time, as well as a small factor due to attenuation

by Rayleigh scattering. That is, the photon flux arriving at the PMT at wavelength λ is (since aerosol attenuation is negligible at the balloon altitude)

$$F_\lambda = F_{\lambda,0} e^{-\alpha_\lambda \mu x - \beta_\lambda \mu p/p_0} \qquad (1)$$

where α_λ and β_λ are the ozone absorption and Rayleigh attenuation coefficients, μ is the airmass ($\sim$sec SZA), $F_{\lambda,0}$ is the flux at the top of the atmosphere, x is the total amount of ozone in a vertical column above the balloon, and p and p_0 are pressure at the balloon altitude and standard atmospheric pressure, respectively. However, the spectrometer at altitude is exposed to strong solar heating and a near-vacuum, making temperature control difficult. During M2002 the internal temperature of the spectrometer changed by more than 20 C. The responsivity of the spectrometer changes with temperature, since temperature affects the electronics (the high-voltage supply and the pulse amplifier/discriminator circuit) and to a lesser extent the $NiSO_4$ crystal filter and the UG-11 glass, and to a very small extent, the photocathode efficiency of the EMI 6256 PMT. In addition, there may be wavelength-dependent changes in responsivity with temperature, since temperature changes in the filters and the photocathode may affect the responsivity differently at different wavelengths.

Using the ratios of sun spectra eliminates $F_{\lambda,0}$. We therefore fit the ratio

$$\log(F_\lambda/F_{\lambda,R}) + \beta_\lambda(\mu - \mu_R)p/p_0 = -\alpha_\lambda(\mu x - \mu_R x_R) + \xi + \eta K(\lambda) \qquad (2)$$

where the R subscript indicates the reference spectrum (the mean of scans #392 and 393), and ξ and η are parameters that allow for overall, and wavelength-dependent changes in responsivity with temperature between spectra. ξ and η are constants and $K\lambda$ is a linear function that is zero at the center of the wavelength range (305 nm) and has values ± 1 at the ends (311.5 and 298.5 nm). For the ozone absorption coefficients α_λ we use the values of Brion et al. [20], interpolated to 263 K.

The Rayleigh-scattering term represents a small correction that is easily calculated. Our extensive experience with the Brewer MkII spectrometers, which have identical filters and PMT to the balloon instrument, and which are characterized regularly for spectral changes in responsivity with temperature, leads us to expect that the correction $\eta K(\lambda)$ should be very small. In fact, the ratio of the responsivity at 298 nm to that at 312 nm derived from (2) for the 13 scans here shows no dependence on temperature.

The correction described by ξ is, however, significant. Fig. 3 shows the mean response of the spectrometer as determined by the spectral fitting, plotted against temperature. A well-defined linear dependence on temperature is evident, with a gradient of $-0.91\% \, \mathrm{K}^{-1}$. This is more than twice the typical temperature dependence of a Brewer, likely due to the Cockroft–Walton high-voltage supply (the Brewer uses a conventional supply), chosen (see Appendix) to reduce thermal dissipation near the PMT.

The calculated ozone slant columns for the 13 scans are listed in Table 2. For each scan all 11,554 data points were used, and the uncertainties (regression error) shown have been adjusted to account for over-sampling due to the 71-pixel width of the spectrometer slit function. Another, occasionally larger, source of uncertainty comes from the $1°$ uncertainty in the derived azimuth pointing data. This was estimated by adding $1°$ to the azimuth pointing error when calculating the azimuth error correction. Two sets of calculated ozone slant columns are shown: the L1 fits are with $\eta = 0$ in (2) and L2 is with η as a free parameter. It should be noted that the addition of ξ and η as free parameters in the fitting, while correcting for temperature-induced errors, is not without cost. For the L1 fit this is equivalent to estimating ozone using an ozone absorption spectrum that is de-trended by subtracting the mean absorption. For the L2 fit, it is equivalent to subtracting a linear fit in wavelength. In comparison to an (ideal) instrument whose responsivity is constant, this implies a loss of sensitivity to ozone that can be estimated from the magnitudes of the effective (de-trended) absorption coefficients,
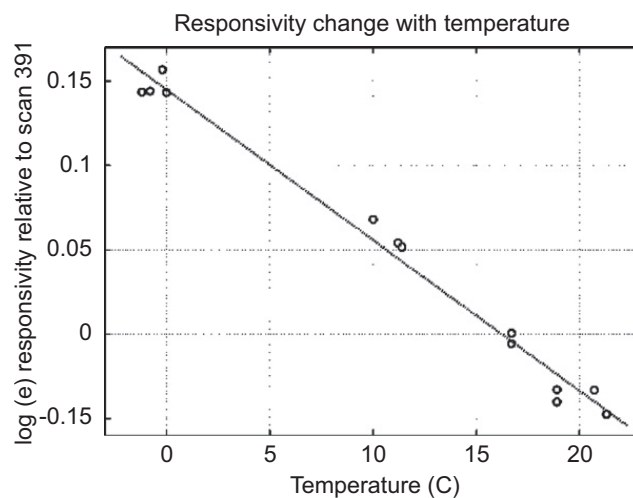

Fig. 3. Results from the L1 spectral fitting illustrating the behavior of the mean responsivity. A well-defined linear dependence with temperature is found, with a gradient of $-0.91\% \, \mathrm{K}^{-1}$. The regression omits the points from scans #502 and 503 which are clearly outliers.

Table 3
Ozone retrievals and standard uncertainties modeled for a curved earth, assuming a scale height of 8 km above 693 Pa

	L1 ozone		L2 ozone	
	O_3	Std	O_3	Std
Ozone mixing ratio (ppmv) above 421 Pa	4.99	0.40	4.48	0.68
Ozone mixing ratio (ppmv) from 693 to 421 Pa	7.08	0.37	7.30	0.63
Ozone (DU) above 693 Pa	32.22	0.65	30.99	1.06
Ozone (DU) above 421 Pa	16.78	1.33	15.07	2.30
Ozone (DU) 693 to 421 Pa	15.44	0.80	15.92	1.38

specifically by factors 2.2 for L1 and 9.4 for L2. As noted, no spectral dependence on temperature was found, and the results of the two sets of fits are similar, except that the errors for the L2 fitting are much larger. In general, the regression error is larger than the azimuth error.

Table 2 also lists pressure levels and air mass factors (μ) for the 13 scans. During the morning the payload descended from 421 to 474 Pa while the sun rose from $\mu = 1.73$ to 1.43 (SZA from 54.8 to 45.6°); in the afternoon it descended further with the last scan at 693 Pa with a μ value of 3.52 (SZA of 73.5°). This profile of measurements evidently has sensitivity to the ozone distribution between 693 and 421 Pa and to the total amount above 421 Pa. As the viewing geometry is precisely known it is a simple matter to construct a set of equations from the ozone slant columns with these two parameters as unknowns and to retrieve a two-parameter ozone distribution. Table 3 shows the results of this, assuming a constant mixing ratio in each layer, applied to the data in Table 2. As with the previous analysis, the L2 uncertainties are larger than those from the L1 method; in this case the ratio is roughly 2.5. However, the results from the two methods are consistent, as the differences are generally smaller than, and always of similar order to, the L2 uncertainties.

The retrieved mixing ratios are sensitive to the mixing ratio profile assumed in the model. Assigning a gradient that is linear in pressure to the mixing ratio in the lower layer, such that the mixing ratio at 693 Pa is 20% higher than at 421 Pa, changes the derived average mixing ratios by −6.3% above 421 Pa and +3.5% between 421 and 693 Pa. These changes are similar in size to the L1 uncertainties in Table 3. Higher-order (i.e. quadratic) modifications of the model profile shape show smaller perturbations in the retrieved values, the quadratic being less than 25% of the linear for a 20% (peak) change. Changes in the assumed profile in the upper layer have very small effects, which are second-order effects of the earth's curvature. (The effect of disregarding the curvature entirely is small, decreasing the retrieved mixing ratios by 2.5% and 0.6%.) For later use in modeling of the strong polarization radiance measurements, we can therefore assume a continuous profile by setting the ozone mixing ratio above 421 Pa to be $7.08(p/421)^{0.422}$, which integrates to the required 16.78 DU, and 7.08 ppmv between 421 and 693 Pa.

The OSIRIS instrument on the ODIN satellite has acquired extensive data on upper stratosphere ozone, which for August/ September at 50°N show maximum differences of ~2% between 421 and 693 Pa [21]. This suggests that the simple model with constant mixing ratio in the lower layer may adequately represent our data.

6. A comparison of extraterrestrial spectra

With an accurate measurement of ozone above the balloon, any of our solar spectra could be used to derive an extraterrestrial solar spectrum at the resolution of our instrument. Scans #392 and #393 from M2002 were chosen for this purpose, the slant column ozone overburdens being, respectively, 27 and 28 DU with standard uncertainties of 2 DU. Fig. 4 shows a very simple comparison of the result with the widely-used spectrum derived by Chance and Spurr [22] from the ground measurements of Kurucz et al. [23] and balloon measurement of Hall and Anderson [24]. The Chance–Spurr (CS) spectrum, which is tabulated at 0.01 nm intervals, was first smoothed with the slit function (black curve) shown in Fig. 1; then it was multiplied by a fourth order polynomial in wavelength, also shown in Fig. 4, chosen to minimize the rms difference between the two spectra.

This comparison is moderately satisfactory and useful for a number of reasons. No absolute radiometric calibration is available for the spectrometer, and the smooth multiplier curve of Fig. 4 provides the variation of the spectrometer's responsivity with wavelength, albeit with the diffuser in place. Specifically the comparison with the CS spectrum indicates that during M2002 the spectrometer's responsivity varied by only 4.7% over the OH measurement range (306–311 nm). A similar comparison with the extraterrestrial spectrum of Thullier et al. [25] shows a 2.5% variation; either result allows the variation to be disregarded for the OH measurement. The measurement of the atmospheric OH does not in principle require knowledge of the absolute responsivity since the OH radiation is compared with the Rayleigh scattering, and both are proportional to the solar radiation.

The match between the CS and the M2002 spectra can be slightly improved by applying a small degree of wavelength shift to the latter. Fig. 5 shows the derived M2002 wavelength shift components, which are 4th degree polynomials in wavelength, in global fits including both amplitude and shift. Between the two calibration wavelengths, the shifts are less
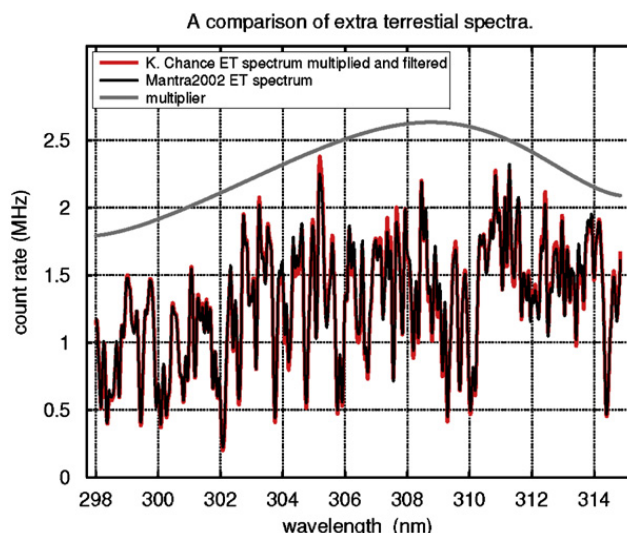
Fig. 4. A measured solar spectrum at 37 km, compared with the spectrum of Chance and Spurr (1997). The CS spectrum, which is tabulated at 0.01 nm intervals, was first smoothed with the slit function (black curve) shown in Fig. 1; then it was multiplied by a fourth order polynomial in wavelength, also shown, chosen to minimize the rms difference between the two spectra.
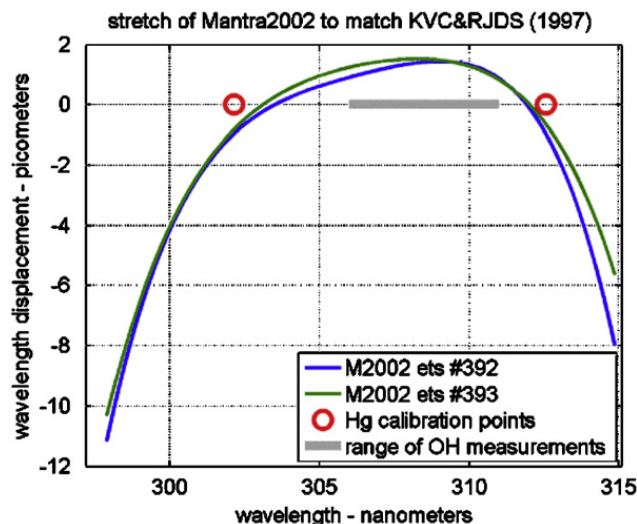

Fig. 5. Derived M2002 wavelength shift components, which are fourth degree polynomials in wavelength, in global fits including both amplitude and shift. Between the two calibration wavelengths, the shifts are less than 0.002 nm.

than 0.002 nm, well within the above-stated maximum wavelength uncertainty, 0.010 nm, for M2002. The same analysis on a revision of CS, kindly provided by Chance, shows virtually identical wavelength shifts and somewhat better agreement in the variation of relative responsivity (0.5% rather than 4.7%).

7. OH spectrum

The OH $A\,^2\Sigma$–$X\,^2\Pi$ transition has been extensively studied and the spectroscopic constants are well known [26,27], as also are the polarization properties of OH scattered radiation which are particularly well described by Zare [28]. It is therefore possible to calculate accurately the emission spectrum or absorption spectrum for a given temperature, since these depend only on the thermal energy distribution in the emitting or absorbing state ($^2\Sigma$ or $^2\Pi$). At temperatures encountered in the stratosphere (200–300 K) about 99% of the energy is contained in fewer than 60 lines and the linewidths are Doppler-determined. If the intensity of incident radiation is uniform throughout the 306–311 nm range or if its values at the specific absorbing wavelengths are known (Cageao et al. [29] give estimates for all lines up to $J = 15.5$), the spectrum and polarization of the scattered radiation can also be calculated. Fig. 6 shows such a spectrum for 250 K. This is the scattered radiation originating from unpolarized flat-spectrum incident radiation, observed at 90° from the direction of the incident radiation. Only the polarization component with electric vector in the scattering plane is shown, which is the polarization direction that coincides with the minimum intensity of Rayleigh scattering (the "weak" polarization).
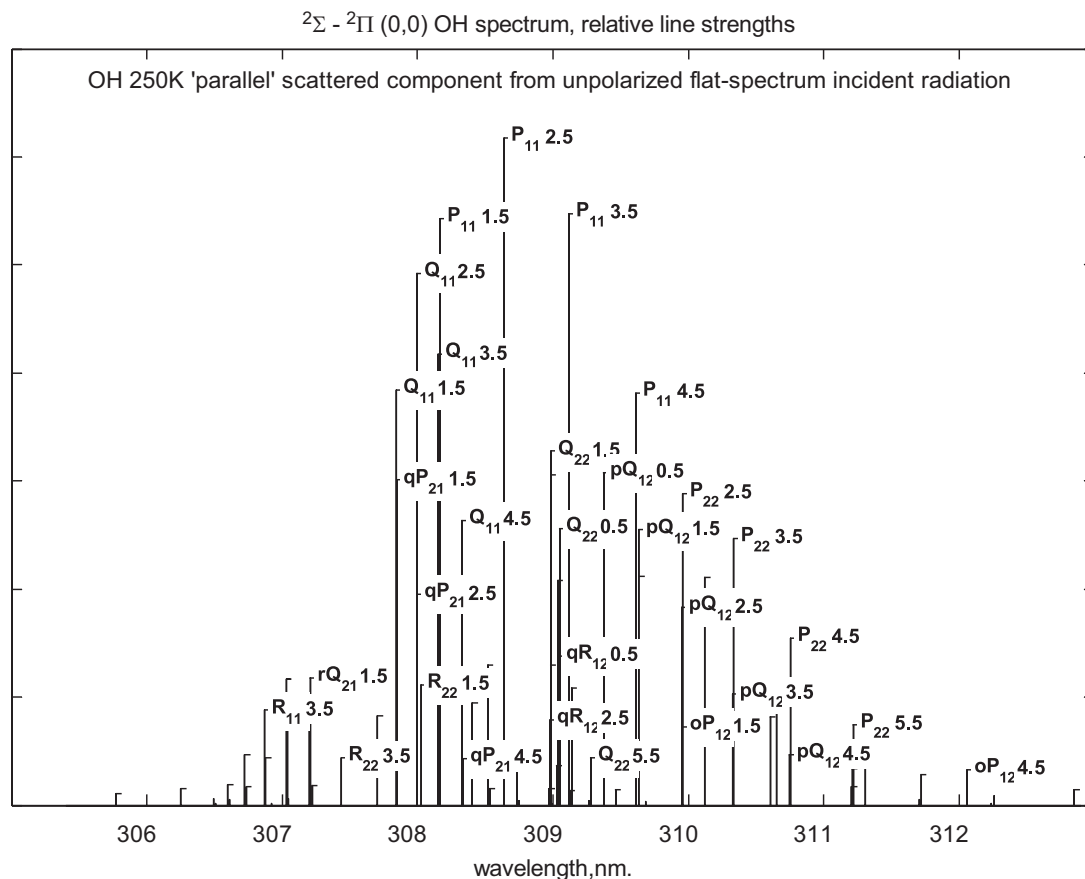
Fig. 6. Calculated OH scattering spectrum for 250 K, for the polarization component with electric vector in the scattering plane (the "weak" polarization), at 90° from the direction of the incident radiation. Unpolarized flat-spectrum incident radiation is assumed.

Fig. 7 shows the spectrum of Fig. 6, as well as the spectrum of scattered radiation in the other polarization (electric vector normal to the scattering plane; the "strong" polarization), and the OH 250 K emission spectrum, each convolved with the slit function (black curve) shown in Fig. 1. The similarity between these two suggests that the scattered radiation is largely unpolarized. A more sophisticated simulation would include the details of the incident solar spectrum; however, it is evident that there are only minor differences between these spectra once convolved with the slit function for the spectrometer (replicating numerically what the spectrometer does physically). The effect of temperature changes from 230 to 270 K on the emission spectrum is shown in Fig. 8. Differences are again minor. The actual atmospheric spectrum due to OH at a given time and viewing direction will be some combination of these spectra. However, given the qualitative similarity of them at our spectral resolution, we can use the OH emission spectrum for 250 K as our "reference" spectrum in our analysis of the OH signal, since it appears unlikely that our measurements contain any significant information on the differences between this spectrum and the actual atmospheric OH spectra.

The detection of OH takes advantage of the OH radiation not being strongly directional or polarized while the Rayleigh scattering is both. Since air molecules are not isotropic, there is a small amount (about 1%) of Rayleigh-scattered sunlight with electric vector in the scattering plane [30]. Rotational Raman scattering of sunlight also results in a small amount of unpolarized scattered light [31]. The weak spectrum will therefore include contributions from the strong spectrum, from the solar spectrum convolved with the Raman-scattering function and from atmospheric OH with a spectrum close to that of emission at 250 K.

The OH signal was inferred by fitting the observed weak spectrum (Fig. 9) with a linear combination of the strong spectrum, the Raman-scattered spectrum, and smaller correction terms formed by multiplying the strong spectrum and an arbitrary constant by polynomials in wavelength. The Raman-scattered spectrum was calculated by convolving the Raman-scattering function with the measured strong spectrum (not the solar spectrum, although this was also measured, since the difference in viewing geometry would introduce differences in ozone absorption). Since the strong and weak spectra are the same width, in order to calculate the Raman-scattered spectrum over the whole width of the weak spectrum, the measured strong spectrum was extended by a simple transformation of the measured solar spectrum. The correction terms are required to remove low-frequency variations in the relative strengths of the weak and strong spectra, which may be caused by ozone-dependent differences between the strong and solar spectra and a wavelength-dependent variation in stray light sensitivity within the instrument. It was found that corrections of higher order than a quadratic multiplier of the strong spectrum and a cubic multiplier of the arbitrary constant made no change to the derived OH signal, and so are not
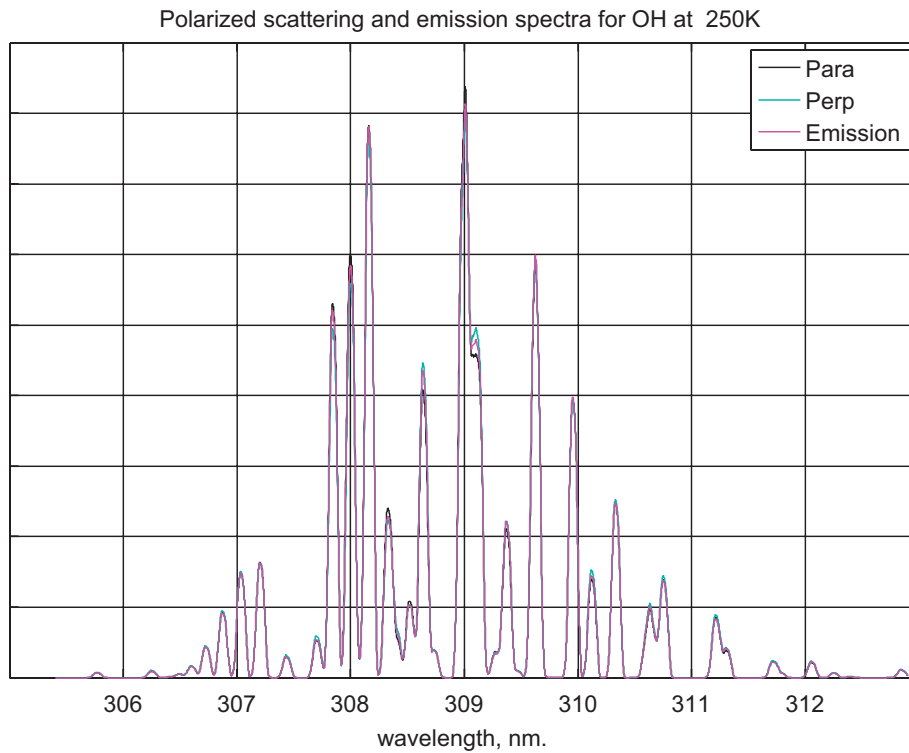
Polarized scattering and emission spectra for OH at 250K

Fig. 7. Spectrum of scattered radiation of Fig. 6 (parallel), as well as the spectrum of scattered radiation in the other polarization (perpendicular) and the OH 250 K emission spectrum, each convolved with the instrument slit function.
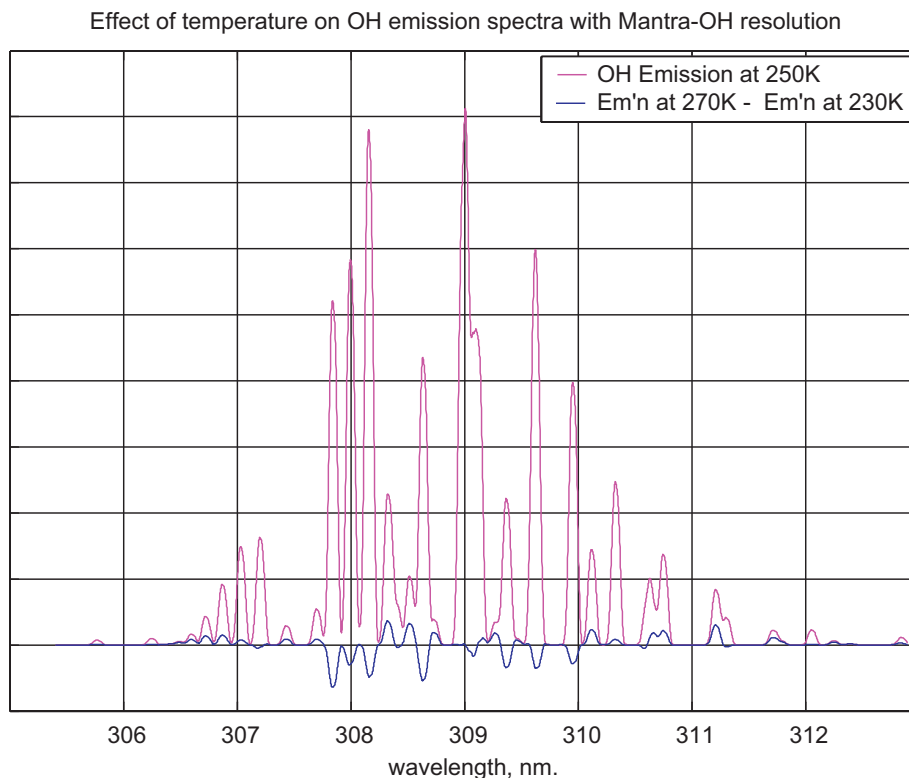
Effect of temperature on OH emission spectra with Mantra-OH resolution

Fig. 8. The OH emission spectrum for temperatures from 230 to 270 K, convolved with the instrument slit function. The difference spectrum is also shown.

included. Two examples of the result of this fitting are shown in Fig. 10, as well as the final residuals after fitting. The initial spectrum for each is the sum of four weak scans, both sets from the same OH measurement group (set of four "weak" scans bracketing two "strong" scans). The upper spectra (green and blue) are two examples of the residuals after the removal of
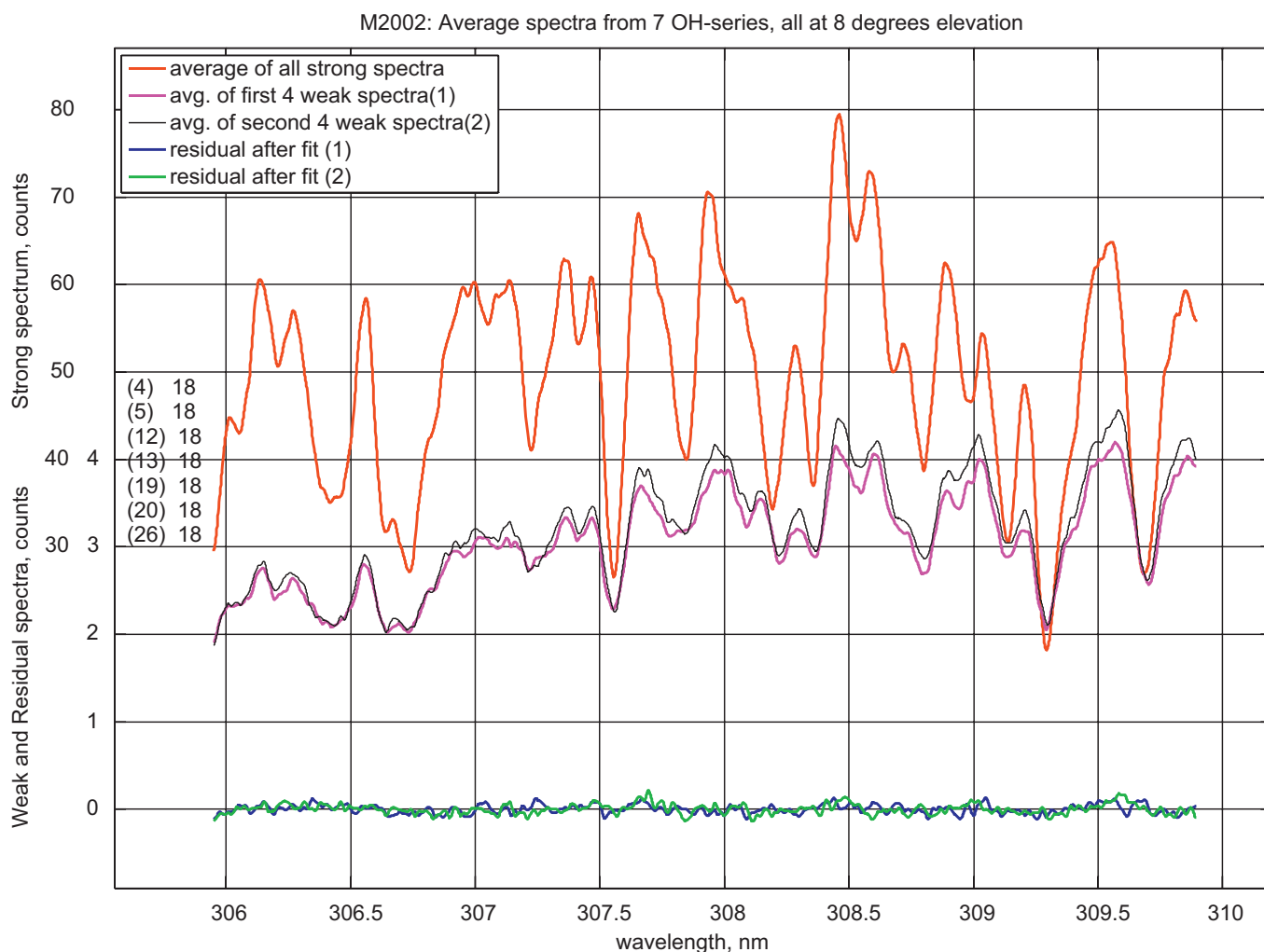
Fig. 9. Examples of the observed weak spectrum, a typical strong spectrum, and the residual after spectral fitting. Each of the two weak spectra is the sum of four weak scans.

all but the OH spectral component. The OH 250 K emission spectrum of Fig. 7 is also shown (pink and red). The OH signal is clearly apparent in these spectra. The lower spectra are the final residuals after the OH spectrum is included in the fit.

The same spectral fitting was applied to derive one OH measurement from each measurement group, in general using all eight weak scans. About 5% of the weak scans were rejected due to instability in the payload azimuth control. In order to express the resulting values for the OH signal in intensity units, knowledge of the spectrometer's absolute radiometric sensitivity is required. This was obtained by comparing the measurements of the sky in the strong polarization setting with values calculated from the revised Chance extraterrestrial spectrum. This was done with a simple fast radiative transfer model using the Rayleigh scattering and depolarizing coefficients of Bodhaine et al. [32], and the more complex VECTOR (VECTor Orders-of-scattering Radiative transfer) model [33,34]. The latter was used to verify the single scattering calculations of the fast model and to provide a lookup table of the contribution from multiple scattering to the measured strong signal. Multiple scattering was found to contribute between 1% and 7% to the measured strong signal. Ozone absorption below the balloon was calculated using data from ozonesondes. Other model inputs included a surface albedo of 0.2 and a background aerosol profile from a SAGE II climatology.

The measurements of the strong spectra (35 in 2002 and 28 in 2004) span a range of solar elevations, viewing angles and pressures, and so a wide range of intensities. The measurement data, the mean counts corrected for temperature response in two wavebands centered at 306.25 and 309.55 nm, were fit to their calculated values, with the regression allowing as free parameters the responsivities for each waveband, a multiplier of the ozone profile above the payload, and an offset (in elevation) to the viewing direction. The ozone profile above the payload for M2002 was that deduced in Section 5, and for M2004 the profile was assembled from MLS data obtained within 200 km and 24 h of the flight.

The results are quite satisfactory, as the comparison of the calculated and measured strong intensities in Figs. 11 and 12 demonstrates. The last four series of the M2004 data were not used in the fitting, as the azimuth pointing control had already failed when these measurements were made. However, these data can still be used to retrieve OH because the OH radiation measurement is not so strongly dependent on accurate orientation or polarization settings. Table 4 gives details of the fitting results.
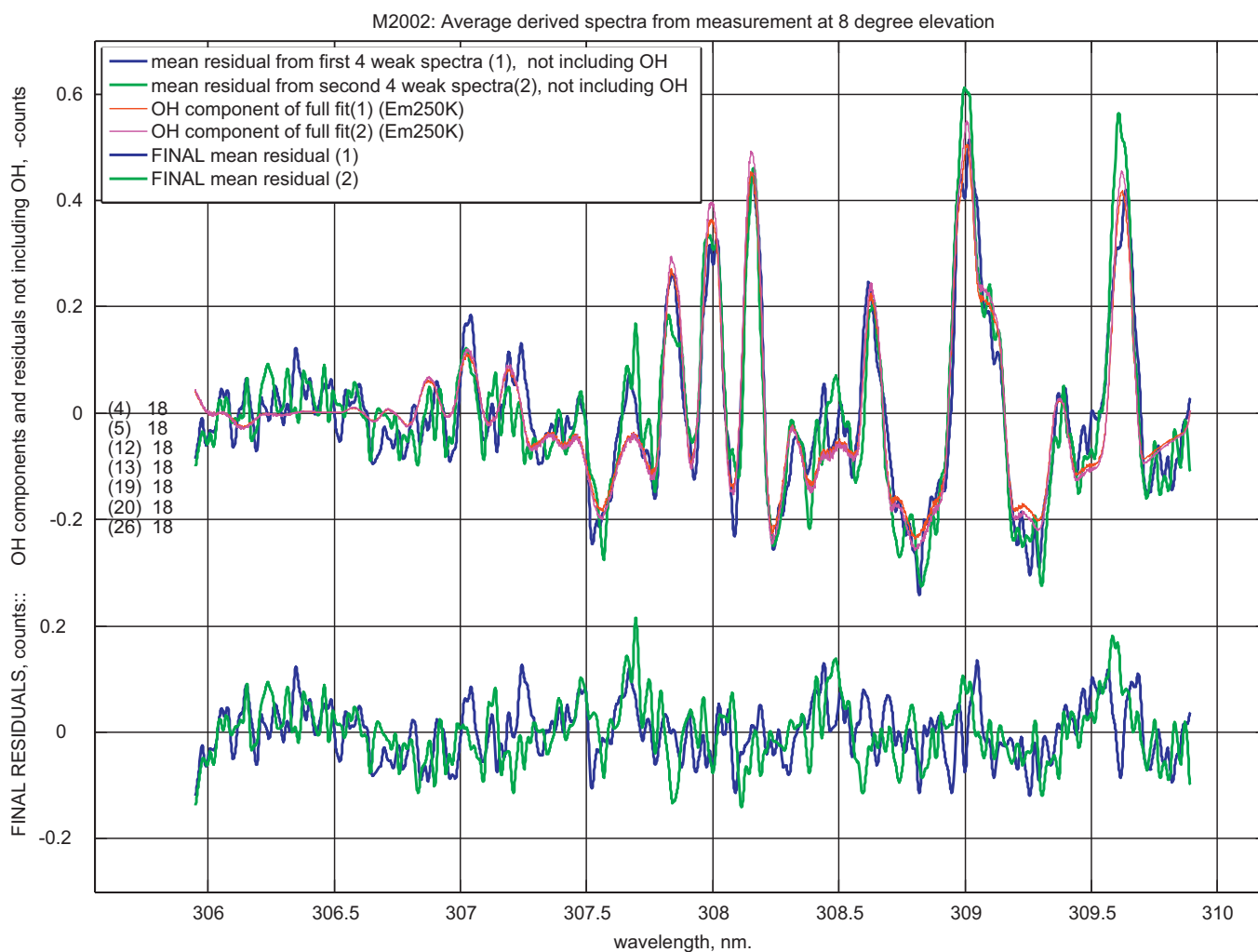
Fig. 10. Upper spectra: residuals after fitting the observed weak spectra with a linear combination of the strong spectrum, the Raman-scattered spectrum, and smaller correction terms formed by multiplying the strong spectrum and an arbitrary constant by polynomials in wavelength. Each of the two initial spectra is the sum of four weak scans. The OH 250 K emission spectrum of Fig. 7 is also shown (pink). The OH signal is clearly apparent in these spectra. Lower spectra: residuals after the OH spectrum is also removed.

The rms residuals are less than 1% of the mean values, and are attributable in part to photon counting statistics (0.3%) as well as to error in the polarization settings, and in the initial response correction for temperature. The differences in estimated responsivity for the short and long wavebands are, respectively, 0.6% and −0.4% for M2002 and M2004 and may be neglected when measuring the OH spectrum. The M2002 difference is within 0.3% of what is obtained when comparing the same revised Chance extraterrestrial spectrum with the M2002-derived instrument extraterrestrial spectrum.

The best agreement with the set of measured spectra (which cover a range of solar elevations) was achieved by assuming an error in the viewing elevation above the horizontal of 0.1°, well within the estimated accuracy of the clinometer alignment relative to the spectrometer's optical axis.

The ozone enhancement value of 4.3% for M2004 is quite reasonable given the geographic and temporal separation between the payload and the MLS data from which the assumed ozone distribution was derived. In contrast, the 7.9% enhancement for M2002 is surprising, since the radiance and ozone measurements are made from the same platform and the total ozone above 693 Pa is determined with a standard error of only 2%. This enhancement can be eliminated by assuming an error of 55 Pa in the pressure at float altitude; however, this is about twice the maximum likely error in pressure, which is based on two pressure and temperature sensors as well as GPS altitude information from two sensors. However, horizontal variability in the ozone distribution may contribute to the difference, since the strong measurement is made at 90° in azimuth from the direct sun ozone measurements, and perhaps more importantly, the latter were made over the 300 km flight path at float of M2002, while the retrieval from them of the ozone distribution, via Eq. (2), assumes that the distribution is constant.

We use the absolute radiometric calibration (responsivity) derived above to express the OH signal in Rayleighs (10^6 photon s^{-1} sr^{-1} cm^{-2}). The results for the 35 OH series on the M2002 flight and the 28 OH series on the M2004 flight are shown in Figs. 13 and 14. The major uncertainty in the radiometric calibration is in knowledge of the absolute pressure, and the maximum likely error in this of about 25 Pa implies an error of about 4% in the estimated responsivities; including
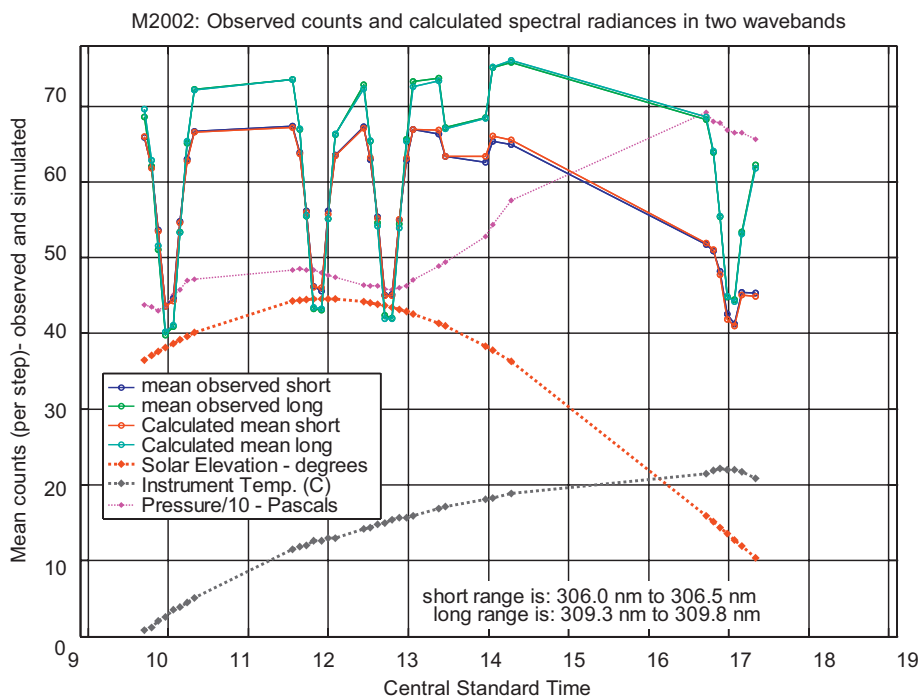
Fig. 11. Comparison of the calculated and measured strong intensities for the 35 measurements of the sky radiance in the "strong" polarization in M2002.
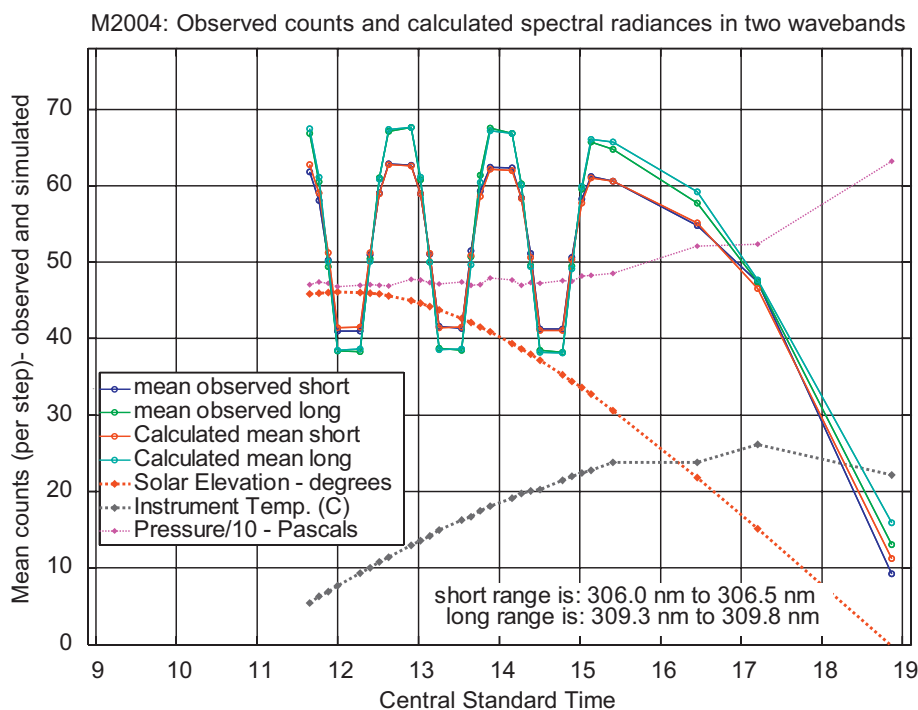

Fig. 12. Comparison of the calculated and measured strong intensities for the 28 measurements of the sky radiance in the "strong" polarization in M2004.

the rms residuals of the fitting above this implies an overall uncertainty to these measurements of about 5%, not including the uncertainty in the absolute radiometric calibration of the extraterrestrial solar spectrum.

These airglow intensities are of course dependent on our definition of the reference spectrum for OH as the 250 K emission spectrum. This is probably quite close to the real atmospheric spectrum, as OH is collisionally dominated below 50 km. However, ozone in the observation path affects not only the overall intensity observed, but also the shape of the observed spectrum, since ozone absorption is greater at the shorter-wavelength end of the spectrum. This can be expected to degrade the quality of the spectral fit, and also possibly to differences in the retrieved OH intensities that depend on ozone in the path, quite apart from the real differences in intensity caused by ozone absorption (which, like self-absorption by ground-state OH, reduces the actual intensity received by the spectrometer). This additional error can be modeled, and

Table 4

Estimated instrument responsivity in two wavebands derived from fitting observed strong spectra to modeled spectra using the revised Chance extraterrestrial spectrum

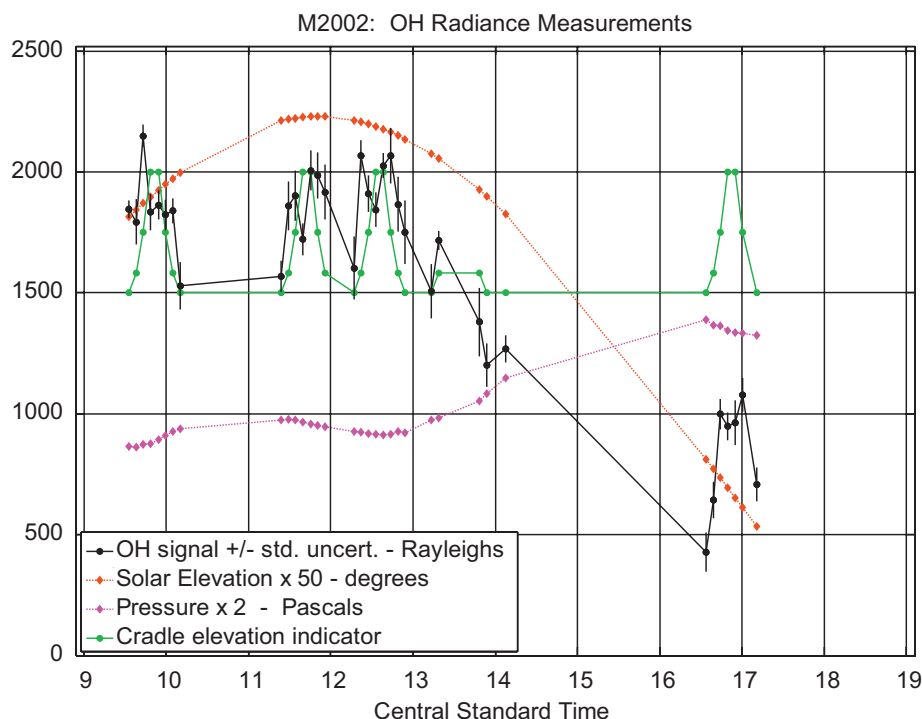|	M2002		M2004	
Wavelength of band center (nm)	306.25	309.55	306.25	309.55
Mean intensity (counts)	55.82	59.06	53.27	53.99
SD (counts)	8.93	11.60	8.25	11.08
rms residuals of fit (counts)	0.35	0.43	0.48	0.44
Responsivity (counts/photon $s^{-1}\,sr^{-1}\,cm^{-2}$)	2.280×10^{-7}	2.262×10^{-7}	1.962×10^{-7}	1.970×10^{-7}
Elevation offset (°)	+0.1		+0.1	
Ozone multiplier	1.079		1.043	

Fig. 13. The OH radiance for the 35 OH series on the M2002 flight. In general each OH radiance measurement is derived from eight weak scans.

is found to result in an underestimation of the OH intensity by typically 1–2%, with a maximum of 6–10% for the two observations in M2002 when the viewing elevation angle was 3° and the pressure was 700 Pa.

There are several previous observations of the OH $A\,^2\Sigma$–$X\,^2\Pi$ (0–0) airglow emission in the literature. Anderson [2,35] reports vertical column intensities of about 700 and 1000 R, respectively, from rocket flights at twilight in April and June, 1971. These amounts agree with our measurements near sunset. Radiance profiles from the space-borne MAHRSI instrument indicate about 140 kR at a tangent height of 50 km [6], which, allowing for a typical line-of-sight enhancement of about a factor of 40, implies an average vertical column intensity of about 3.5 kR. Our results could be expected to be slightly lower, since the maximum float altitude of the balloons was about 37 km, and absorption by ozone as well as self-absorption by ground-state OH should reduce the number of OH photons detected at this altitude. The MAHRSI observations also indicate a diurnal variation in intensity similar to that seen in our results; that is, a modest variation with SZA until near sunset, with a rapid fall-off in twilight. The measurements in the literature most similar to ours are those of Torr et al. [4], who measured the OH $A\,^2\Sigma$–$X\,^2\Pi$ (0–0) emission from a balloon platform at 40 km in August 1983 and June 1986 near Palestine, Texas. They report intensities that are several times higher than reported here (9–13 kR for similar viewing conditions). While the OH emission should be somewhat brighter at 40 km than at the slightly lower altitudes of our measurements, the magnitude of the difference is surprising.

8. Conclusions

The measurement of OH in the middle atmosphere is quite challenging and there exist relatively few observations of the radiation from, or the atmospheric concentration of this important trace species. Such measurements, however, are quite
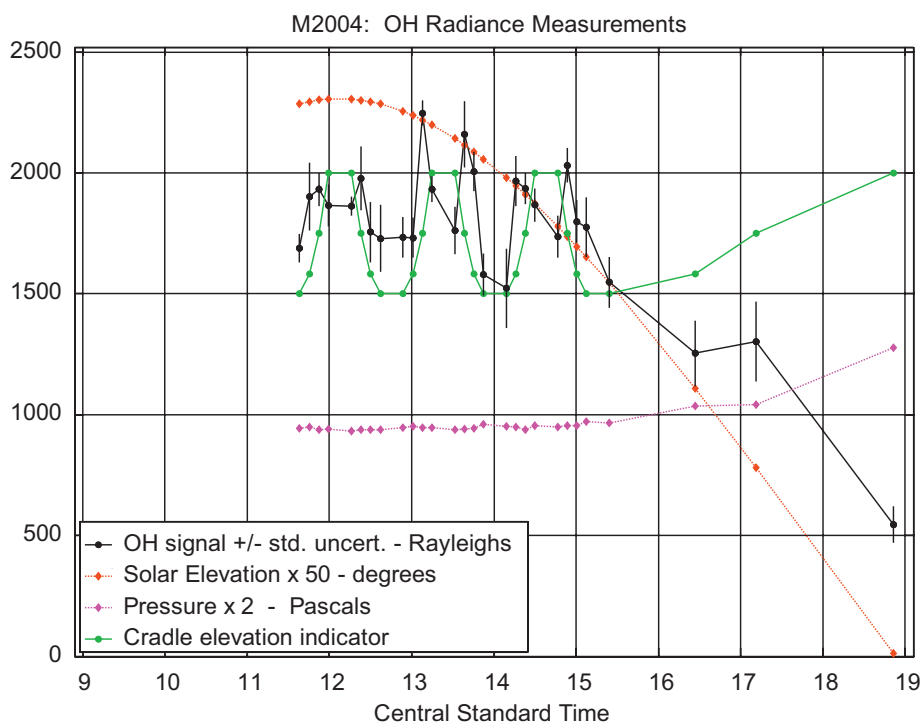
Fig. 14. The OH radiance for the 26 OH series on the M2004 flight. In general each OH radiance measurement is derived from eight weak scans.

important, as the hydroxyl radical is the most important oxidizing agent in the middle atmosphere, and OH chemistry dominates ozone destruction above about 40 km [1].

A moderately high-resolution grating spectrometer designed to measure solar radiation in the spectral range 295–315 nm was flown on the MANTRA payloads of 2002 and 2004. Despite problems with the payload azimuth control system, and (on M2004) loss of command telemetry, we are able to derive useful measurements of the solar UV spectrum at altitude, the amount of ozone above the balloon, and the OH spectrum retrieved from the scattered radiation measurements.

Detailed attention has been paid to in-flight characterization of the spectrometer, particularly wavelength calibration and dispersion. The direct sun measurements have been analyzed both to characterize the spectrometer responsivity to scattered radiation and to estimate the ozone abundance at the flight altitude and above. Uncertainties in wavelength calibration, responsivity, azimuth pointing and ozone overburden are estimated. A high-resolution solar spectrum at 37 km altitude extrapolated to space compares quite well with others in the literature, and permits some degree of confidence in our error analysis. A typical observed OH spectrum, as well as the complete set of observed OH $A\ ^2\Sigma$–$X\ ^2\Pi$ (0–0) airglow emission measurements are presented. We estimate the precision of these intensity measurements to be about −5% to +10% (1σ), plus any additional uncertainty in the absolute radiometric calibration of the extraterrestrial solar spectrum.

Given the necessary atmospheric data the full spectrum of OH radiation can be calculated, allowing for absorption of the incident and scattered radiation by ozone and self-absorption of the scattered radiation by OH molecules. The calculation also requires the strengths of solar radiation at the individual OH wavelengths. These strengths are not available from our measurements, but have been estimated from much higher wavelength resolution observations (e.g. [29]). This will allow us to accurately model the OH radiation as measured by our instrument, and thereby to derive accurate estimates of the OH concentration, and to compare with other OH measurements and with model data.

Acknowledgments

Appendix. Detailed instrument design

The spectrometer layout is of the most simple Ebert–Fastie type [17]. The centers of the entrance and exit slits, and those of the collimating and focusing mirrors define the principal plane, which is vertical. The entrance and exit slits are

separated by 216 mm in the vertical, as are the mirrors, and the horizontal distance from either slit to the corresponding mirror is 600 mm. The grating is located centrally, about 6 cm in front of the slits, so that the light path is an "M" in the vertical plane. The grating has a line density of 1200 lines mm^{-1} with blazing for 1.0 μm; it is used in the third order. The mirrors have a radius of curvature of 1200 mm. The entrance and exit slits are curved with a radius of 240 mm; they are 12 and 20 mm long and approximately 0.15 and 0.20 mm wide, respectively. With this simple geometry the center directions of the entrance and exit light beams are parallel and normal to the plane containing the slits, and the geometric width of either slit is equivalent to about 0.055 nm.

The grating is held in an aluminum block whose axis of rotation is defined by crossed wires on either side of the block; horizontal movement is prevented by a similar wire aligned along the axis of rotation, fixed both in the grating block and on the spectrometer frame. The rotation angle is controlled by a motorized micrometer pushing a rod which pushes an arm attached to the grating block. The micrometer tip and the arm contact are both conical with rounded tips. These tips rest in small pyramid indentations made by a pressing a cube corner into the brass ends of the rod. The effective arm length and rod length are 370 and 210 mm, respectively. The resulting wavelength dispersion is equivalent to approximately 870 motor steps per nm, changing by about 2% between 302.1 and 312.6 nm. The zero-step position is defined by the signals from two LED–photodiode pairs, sensing, respectively, the rotation and the translation of the micrometer.

Following the exit slit, the detector optics comprise a collecting lens and two filters, one of UG-11 glass and one a 10 mm-thick crystal of $NiSO_4 \cdot 6H_2O$, to suppress response to radiation with wavelengths longer than 320 nm. This glass and crystal filter combination is the same as used in the Mark II Brewer ozone spectrophotometer, where it is found to be effective in suppressing longer-wavelength radiation [36,37]. The lens, of focal length 38 mm and diameter 38 mm, is immediately behind the exit slit and images the grating, and consequently the aperture stop, onto the 10-mm-diameter sensitive area of the PMT detector. The aperture image diameter is ~6 mm.

The PMT, an EMI 6256, is used in the pulse counting mode. A pulse amplifier, a pulse height discriminator and a prescaler that divides the photon count by a factor of 4 are all mounted close to the PMT base, as is a Cockroft–Walton voltage multiplier which provides the anode (~1400 V) and dynode voltages. These components with the glass and crystal filters are all mounted in a light-weight, hermetically sealed can, in which the pressure is roughly 110 KPa. The window is the collecting lens. The oscillator for the Cockroft–Walton multiplier is outside the PMT housing, at ambient pressure, and is controlled by feedback from the first stage of the multiplier (inside the PMT housing). This arrangement limits the maximum voltage in ambient pressure to less than 200 V and, compared with putting the oscillator inside the housing, reduces the heat release near the PMT by ~3 W.

The optical components described above are housed in a $1.09 \times 0.39 \times 0.41$ m box, along with an onboard computer, control electronics and internal heaters. The box was partially clad in 25 mm thick rigid foam insulation and wrapped in reflective mylar film (space blanket), in order to avoid excessive solar heating at altitude, and excessive cooling during ascent. Most of the instrument is constructed of rigid aluminum; the overall mass is 36 kg.

The onboard control computer is a TRI-M Systems MZ104, a PC 104 board with a ZF×86 processor and 144 MB flash disk, running Linux. One A/D and two digital I/O boards interface, via a custom signal pretreatment board, to the spectrometer hardware. External communications and control are via two RS232 ports. The computer operates the instrument following a predefined script of commands, recording the data onboard as well as outputting it to one of the RS232 ports (for telemetry to ground). It will also respond to telemetered commands, permitting complete manual control, but on loss of telemetry will switch to autonomous operation.

References

[1] World Meteorological Organization (WMO) Scientific Assessment of Ozone Depletion: 1998, Global Ozone Res Monit Proj Rep 44, Geneva, Switzerland. 1999.

[2] Anderson JG. Rocket measurement of OH in the mesosphere. J Geophys Res 1971;76:7820–4.

[3] McElroy CT, Wardle DI. The detection of OH and ClO in UV spectra of the sky and sun measured by a balloon-borne high resolution spectrometer. In: Proceedings of the symposium on the geophysics aspects and consequences of changes in the composition of the stratosphere. Toronto, 1978. p. 85–90.

[4] Torr DG, Torr MR, Swift W, Fennelly J, Liu G. Measurements of $OH(X^2\pi)$ in the stratosphere by high resolution UV spectroscopy. Geophys Res Lett 1987;14:937–40.

[5] Conway RR, Stevens MH, Cardon JG, Zasadil SE, Brown CM, Morrill JS, et al. Satellite measurements of hydroxyl in the mesosphere. Geophys Res Lett 1996;23:2093–6.

[6] Conway RR, Stevens MH, Brown CM, Cardon JG, Zasadil SE, Mount GH. The middle atmosphere high resolution spectrograph investigation. J Geophys Res 1999;104:16327–48.

[7] Summers ME, Conway RR, Siskind DE, Strobel DF, Zasadil SE. Mesospheric HO_x photochemistry: constraints from recent satellite measurements of OH and H_2O. Geophys Res Lett 1996;23(16):2097–100.

[8] Summers ME, Conway RR, Siskind DE, Stevens MH, Offermann D, Riese M, et al. Implications of satellite OH observations for middle atmospheric H_2O and ozone. Science 1997;277:1967–70.

[9] Conway RR, Summers ME, Stevens MH, Cardon JG, Preusse P, Offermann D. Satellite observations of upper stratospheric and mesospheric OH: the HO_x dilemma. Geophys Res Lett 2000;27:2613–6.

[10] Heaps WS, McGee TJ. Progress in stratospheric hydroxyl measurements by balloon-borne LIDAR. J Geophys Res 1985;90:7913–21.

[11] Stimpfle RM, Wennberg PO, Lapson LB, Anderson JG. Simultaneous, *in situ* measurements of OH and HO_2 in the stratosphere. Geophys Res Lett 1990;17(11):1905–8.

[12] Pickett HM, Peterson DB. Comparison of measured stratospheric OH with predictions. J Geophys Res 1996;101:16,789–96.

[13] Jucks KW, Johnson DG, Chance KV, Traub WA, Margitan JJ, Osterman GB, et al. Observations of OH, HO_2, H_2O, and O_3 in the upper stratosphere: implications for HO_x photochemistry. Geophys Res Lett 1998;25(21):3935–8.

[14] Pickett HM, Drouin BJ, Canty T, Kovalenko LJ, Salawitch RJ, Livesey NJ, et al. Validation of Aura MLS HO_x measurements with remote-sensing balloon instruments. Geophys Res Lett 2006;33:L01808.

[15] Osterman GB, Salawitch RJ, Sen B, Toon GC, Stachnik RA, Pickett HM, et al. Balloon-borne measurements of stratospheric radicals and their precursors: implications for the production and loss of ozone. Geophys Res Lett 1997;24(9):1107–10.

[16] Canty T, Pickett HM, Salawitch RJ, Jucks KW, Traub WA, Waters JW. Stratospheric and mesospheric HO_x: results from Aura MLS and FIRS-2. Geophys Res Lett 2006;33:L12802.

[17] Fastie WG. Small plane grating monochromator. J Opt Soc Am 1952;42:641–7.

[18] Angel JRP, Illing R, Martin PG. Circular polarization of twilight. Nature 1972;238:389–90.

[19] Hansen JE, Travis LD. Light scattering in planetary atmospheres. Space Sci Rev 1972;16:527–610.

[20] Brion J, Chakir A, Daumont D, Malicet J, Parisse C. High-resolution laboratory absorption cross section of O_3. Temperature effect. Chem Phys Lett 1993;213:610–2.

[21] Degenstein DA, Bourassa AE, Roth CZ, Llewellyn EJ. Limb scatter ozone retrieval from 10 to 60 km using a multiplicative algebraic reconstruction technique. Atmos Chem Phys Discuss 2008;8:11853–77.

[22] Chance KV, Spurr RJD. Ring efffect studies: Rayleigh scattering, including molecular parameters for rotational Raman scattering, and the Fraunhofer spectrum. Appl Opt 1997;36:5224–30.

[23] Kurucz RL, Furenlid I, Brault J, Testerman L. Solar flux atlas from 296 to 1300 nm. Sunspot, New Mexico: National Solar Observatory; 1984. 240pp.

[24] Hall LA, Anderson GP. High-resolution solar spectrum between 2000 and 3100 Å. J Geophys Res 1991;96:12927–31.

[25] Thuillier G, Hersé M, Labs D, Foujols T, Peetermans W, Gillotay D, et al. The solar spectral irradiance from 200 to 2400 nm as measured by the SOLSPEC spectrometer from the ATLAS and EURECA missions. Sol Phys 2003;214:1–22.

[26] Stark G, Brault JM, Abrams MC. Fourier-transform spectra of the $A\ ^2\Sigma^+$–$X\ ^2\Pi\ \Delta v = 0$ bands of OH and OD. J Opt Soc Am 1994;B11:3–32.

[27] Luque J, Crosley DR. Transition probabilities in the $A\ ^2\Sigma^+$–$X\ ^2\Pi$ electronic system of OH. J Chem Phys 1998;109:439–48.

[28] Zare RN. Angular momentum: understanding spatial aspects in chemistry and physics. New York: Wiley-Interscience; 1988.

[29] Cageao RP, Ha YL, Jiang Y, Morgan MF, Yung YL, Sander SP. Calculated hydroxyl $A\ ^2\Sigma$–$X\ ^2\Pi$ (0, 0) band emission rate factors applicable to atmospheric spectroscopy. JQSRT 1997;57:703–17.

[30] Herzberg G. Spectra of diatomic molecules. Princeton, NJ: Van Nostrand; 1950. p. 128.

[31] Grainger JF, Ring J. Anomalous Fraunhofer line profiles. Nature 1962;193:762.

[32] Bodhaine BA, Word NB, Dutton EG, Slusser JR. On Rayleigh optical depth calculations. J Atmos Oceanic Technol 1999;16:185–1861.

[33] McLinden CA, McConnell JC, Griffioen E, McElroy CT. A vector radiative transfer model for the Odin/OSIRIS project. Can J Phys 2002;80:375–93.

[34] McLinden CA, Haley CS, Sioris CE. Diurnal effects in limb scatter observations. J Geophys Res 2006;111:D14302.

[35] Anderson JG. Rocket-borne ultraviolet spectrometer measurement of OH resonance fluorescence with a diffusive transport model for mesospheric photochemistry. J Geophys Res 1971;76:4634–51.

[36] Kerr JB, McElroy CT, Evans WFJ. The automated Brewer spectrophotometer for measurement of SO2, O3 and aerosols. In: Proceedings of the WMO/AMS/CMOS Symposium on Meteorological Observations and Instrumentation. 11–15 April 1983, Toronto, Canada, 1983. p. 470–2.

[37] Kerr JB, McElroy CT, Evans WFJ. The automated Brewer spectrophotometer. In: Proceedings of the Quadrennial Ozone Symposium, 3–7 September 1984, Halkidiki, Greece, 1984. p. 396–401.